Desalination and Water Treatment
www.deswater.com

doi: 10.5004/dwt.2019.23465

140 (2019) 212–221
February

Enhanced photocatalytic and Fenton-like performance of Fe-doped MoS_2 nanosheets under visible light irradiation

Cheng Liu, Zhiyong Zhang*, Rui Qu, Wu Zhao, Junfeng Yan

School of Information Science and Technology, Northwest University, Xue fu Street, Xi'an 710127, China, Tel. +86 15191840326; emails: 570015061@163.com, zhangzy@nwu.edu.cn (Z. Zhang)

Received 25 June 2018; Accepted 12 November 2018

ABSTRACT

MoS_2-based transition-metal chalcogenide has attracted increasing research attention due to features of low cost, high activity, environmental sustainability, and a strong visible light response. However, the limited quantity of active sites and high recombination rate of photo-generated charge carriers have hampered the efficiency of photocatalysis. In this paper, a Fe dopant was used to improve photocatalytic performance. XRD, energy dispersive spectrometer mapping, and X-ray photo-electron spectroscopy characterizations demonstrate that Fe atoms were successfully doped into the MoS_2 matrix. The UV–Vis absorption spectra, photocurrent density spectra, electrochemical impedance spectroscopy, and PL spectra indicate that the introduction of Fe dopant effectively improved the quantum yield and suppressed the recombination of photo-generated electrons and holes. In this paper, the as-prepared Fe-doped MoS_2 nanosheets were used to degrade RhB and demonstrated enhanced photocatalytic activity, attributed to the following. First, the introduction of Fe^{3+} dopants formed new active sites in the inert basal plane of MoS_2, which benefits the photocatalytic reaction. Second, the doped Fe^{3+} could trap photo-generated electrons and be reduced to Fe^{2+}, which improved the separation efficiency of photo-generated charge carriers. Finally, a photo-Fenton-like reaction occurred during RhB degradation. Fe^{2+} can also accelerate the decomposition of H_2O_2 and generate active species of ·OH. ·OH can unselectively oxidize organics into CO_2, H_2O, and minerals. Fe^{2+} can also be perpetually regenerated and reused, which could support the long-term application of Fe-doped MoS_2 in water treatment.

Keywords: Fe-doped MoS_2 nanosheets; Enhanced photocatalytic activity; Photo-Fenton

1. Introduction

Water constitutes a key resource for life on Earth [1]. However, modern industries such as textiles, paper, leather, and pharmaceuticals use various organic dyes heavily, 15% of which are released into water bodies [2]. These dyes pose risks to the environment and human health and are difficult to degrade naturally. Many methods such as adsorption [3], membrane filtration [4], sedimentation [5], coagulation [6], and electro-coagulation [7], and the advanced oxidation process (AOP) have been employed for removal or degradation of toxic dyes [8]. Among these, AOP, which can generate reactive oxygen species that subsequently degrade dyes into CO_2, H_2O, and mineral acids [9], is well recognized as a promising technology for wastewater treatment due to its ease of use and high efficiency.

One type of AOP, semiconductor photocatalysts has recently attracted growing research interest and has been widely applied in wastewater treatment because these photocatalysts can be conducted under mild conditions using nontoxic materials, thus presenting economic and environmental advantages [10,11]. Many wide band-gap semiconductor materials (e.g., TiO_2, ZnO, SnO_2, Fe_2O_3, and their composites) have been developed as active catalysts for the photo-degradation of organic pollutants given their excellent chemical stability, low cost, and nontoxicity [12–14]. These

* Corresponding author.

semiconductors can harvest ultraviolet (UV) light and completely degrade organic dyes. Unfortunately, the solar spectrum consists of only 3%–5% UV light, whereas 50% and 47% of the spectrum is composed of visible light and infrared radiation, respectively [15]. Therefore, novel photocatalysts that can harvest visible light for rapid water disinfection is urgently needed in the environmental protection field.

Compared with conventional TiO_2-based photocatalysts, MoS_2-based photocatalysts with a band-gap width of 1.9 eV have attracted considerable attention in the photo-degradation of organic pollutants due to strong absorption in the visible light region, heavy metal-free composites, good chemical stability, and low cost [16]. However, pristine MoS_2 presents problems of limited surface area, poor conductivity, an inert two-dimensional MoS_2 surface, and a high combination of photon-generated carriers [17], rendering it difficult to obtain high photo-degradation performance.

Theoretical calculations and experimental studies have demonstrated that active photocatalytic reaction sites arise from edge planes and rim planes rather than basal planes in MoS_2 nanosheets [18]. Many attempts to further improve the catalytic activity of MoS_2 have focused on increasing the number of active sites and suppressing the recombination of photo-generated carriers. Nano-sized MoS_2 could expose more edge planes and decrease the distance that the electrons and holes diffuse from internal to the surface. For example, Huang et al. [19] prepared defect-rich MoS_2 ultrathin nanosheets, leading to a substantial improvement in hydrogen evolution reaction activity. Composites of MoS_2 and other materials (e.g., graphene, ZnO, C_3N_4, and CdS) were synthesized to improve photocatalytic performance [20–23] because the heterogeneous interface that forms between MoS_2 and other semiconductor materials is beneficial for separating photo-generated electrons and holes.

Generally, most MoS_2 research aims to increase active site exposure by reducing the size of MoS_2 nanosheets, which then increases the cost and challenges associated with synthesis. Recent theoretical calculations on single-layer MoS_2 suggest that in-plane chemical doping of heteroatoms could modulate the electronic structure, produce additional active sites for catalysis, trap photo-generated carriers, and suppress the recombination of photo-generated electron–hole pairs [24–30]. Among various kinds of dopants, Fe possesses varying chemical valence. Especially in the Fenton reaction, the catalytic performance of iron oxide is closely associated with oxidation states. However, Fenton degradation also suffers from numerous challenges such as a high iron-leaching rate and Fe^{2+} regeneration, which can significantly limit reusability and may generate undesired iron sludge during the Fenton process [31–33].

Inspired by these problems, this study designs and successfully synthesizes Fe-doped MoS_2 nanosheets using the one-pot hydrothermal method. Fe dopants may serve as new active sites in the MoS_2 basal plane and improve intrinsic electronic conductivity. At the same time, Fenton degradation is found to occur on the surface of Fe-doped MoS_2 nanosheets because Fe^{2+} can promote H_2O_2 decomposition into hydroxyl radicals (·OH). Photo-generated electrons can be captured by Fe^{3+} and reduced Fe^{3+} to F^{2+}, effectively suppressing the recombination of photo-generated electron–hole pairs and promoting regeneration of Fe^{2+}. In addition, Fe dopants may act as a recombination center to drastically suppress $\cdot O_2^-$ formation at the conduction band (CB) of MoS_2. Fe-doped MoS_2 samples with different doping concentrations were synthesized, and the effects of Fe dopants were systematically investigated. Finally, a possible photocatalytic and Fenton-like mechanism of Fe-doped MoS_2 nanosheets is discussed.

2. Experimental section

2.1. Materials

Sodium molybdate, thiourea, and hexahydrate ferric chloride were purchased from Tianjin Chemical Reagent Co., Ltd. Other chemicals were purchased from Shanghai Chemical Reagent Co., Ltd. All chemicals were of analytical grade and used as received without further purification.

2.2. Synthesis of Fe-doped MoS_2 nanosheets

In a typical synthesis, 1.5 mmol of $Na_2MoO_4{\cdot}2H_2O$ and 4.5 mmol of CN_2H_4S were dissolved into 30 mL of deionized water under vigorous stirring for 10 min and adjusted pH (1) using HCl. Then, a certain amount of $FeCl_3{\cdot}6H_2O$ was added to the above solution and stirred for another 10 min. Finally, the resulting mixture was transferred into a 50-mL teflon-lined autoclave, which was heated at 200°C for 24 h. After cooling naturally to room temperature, the black products were collected and washed carefully with distilled water and ethanol several times. Finally, the products were dried in a vacuum oven at 60°C for 12 h. Fe-doped MoS_2 with various molar ratios of Fe to Mo (0%, 1.1%, 2.9%, 4.3%, and 5.1%) were prepared by changing the molar of $FeCl_3{\cdot}6H_2O$ using a similar process.

2.3. Characterization

Powder X-ray diffraction (XRD) was performed on a Bruker D8 Advance diffractometer at 40 kV and 40 mA for Cu Ka (λ = 0.15406 nm). The morphology and size of the as-prepared Fe-doped MoS_2 were analyzed using a scanning electron micrograph (SEM; ZEISS, and SIGMA/VP) and transmission electron microscopy (TEM; JEOL, JEM-2100). Components of the as-prepared Fe-doped MoS_2 composite were further investigated using X-ray photo-electron spectroscopy (XPS; Physical Electronics PHI5400, USA). The absorbance spectrum and UV–Vis diffuse reflectance spectrum were measured with a UV–Vis spectrophotometer (UV–Vis, U3310; Hitachi Ltd.). Electrochemical properties were assessed using an electrochemical station (CHI 660E; Shanghai, Chenhua, China).

2.4. Active species in the photocatalytic and Fenton-like systems

An active species trapping experiment was used to investigate the active species involved in the photocatalytic process. Ammonium oxalate (OA), 1,4-benzoquinone (BQ), and isopropyl alcohol (IPA) were used as the hole, and $\cdot O_2^-$, and ·OH scavengers were used to identify the main active species [34,35].

2.5. Photo-catalytic performance tests

Photo-catalytic performance of the photocatalyst was assessed based on degradation of the RhB solution. The highest optical absorption of RhB at 529 nm was used to monitor

the photo-degradation wavelength [36]. The temperature of the reaction was maintained at room temperature by circulating water using an Xe lamp (300 W) equipped with a UV cut-off filter ($\lambda > 400$ nm) as the irradiation source. In a typical photocatalytic experiment, at certain time intervals, 5.0 mL of the suspension was withdrawn and centrifuged to remove the Fe-doped nanosheets, and the concentration of the RhB solution was analyzed by recording the absorbance using a UV–Vis spectrophotometer. The degradation capacity η was calculated using the following equation:

$$\eta = \frac{C_0 - C_t}{C_0} \quad \text{(I)}$$

where C_0 is the initial concentration of RhB (mg L^{-1}), and C_t is the equilibrium concentration of RhB at time t.

2.6. Photo-electrochemical experiment

Photo-electrochemical measurements were carried out in a three-electrode quartz glass cell connected to an electrochemical station (CH Instrument 660E; Shanghai, Chenhua, China). Pristine MoS_2/ITO, 1.1 at % Fe-doped MoS_2/ITO, 2.9 at % Fe-doped MoS_2/ITO, 4.3 at % Fe-doped MoS_2/ITO, and 5.1 at % Fe-doped MoS_2/ITO with an effective area of 1 cm^2 were prepared as working electrodes. A Pt wire and an Ag/AgCl (saturated KCl) electrode were used as the counter-electrode and reference electrode, respectively. The electrolyte was the 0.5 mol L^{-1} Na_2SO_4 aqueous solution. A xenon lamp was used as the UV light source. The photocurrents of the working electrodes were maintained at a constant potential of 0.5 V.

3. Results and discussion

3.1. Characterization of Fe-doped MoS_2 nanosheets

Fig. 1 shows the XRD patterns of pristine MoS_2, 1.1 at % Fe-doped MoS_2, 2.9 at % Fe-doped MoS_2, 4.3 at % Fe-doped MoS_2, and 5.1 at % Fe-doped MoS_2 nanosheets. The as-synthesized samples exhibited nearly identical characteristic peaks, indexed to hexagonal MoS_2 (2H-MoS_2, JCPDS 37-1492). Furthermore, with the addition of Fe, no remarkable changes emerged in the XRD patterns or any diffraction

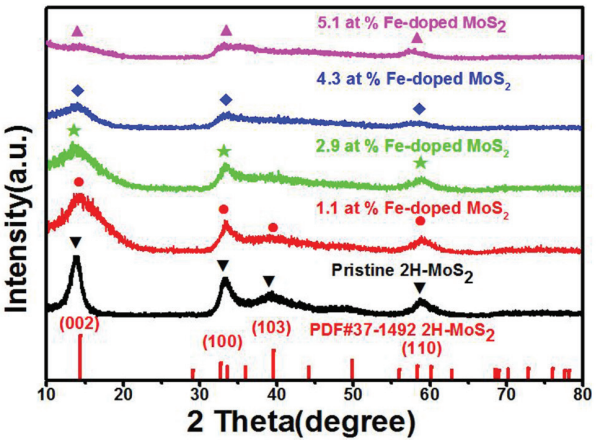

Fig. 1. XRD patterns of pure MoS_2 and Fe-doped MoS_2.

maximum characteristic or ferrous chloride used as a precursor to formulation. Hence, Fe appeared to have doped into the MoS_2 crystals. The XRD peaks of the Fe-doped MoS_2 also seemed broader and weaker in intensity (Fig. 1), indicating a reduction in the average grain size and crystallinity and an increase in defective and disordered structures in the Fe-doped MoS_2 due to open edges after Fe doping.

The morphology and microstructure of the Fe-doped MoS_2 were examined using SEM and TEM. Parts of the nanosheets were assembled into blocks for pure MoS_2, which is not effective in exposing more active sites. However, the addition of iron ions improved the dispersibility of MoS_2 nanosheets. Comparing the SEM images of pristine MoS_2 and Fe-doped MoS_2 (Figs. 2(a) and (b)), the Fe-doped MoS_2 demonstrated a more disordered appearance, indicating disordering of atomic arrangements and reduced crystallinity, which was in agreement with the XRD analysis of the Fe-doped MoS_2 nanosheets.

Energy dispersive spectrometer (EDS) mapping was carried out to verify element distribution. As shown in Figs. 2(c) and (d), the EDS mapping analysis of Fe-doped MoS_2 reveal the presence of Mo, S, and Fe elements, with the Fe element evenly distributed in the sample. The EDS results also show that the Fe content on the surface was 0.65% Fe and Mo content was 22.5%. In total, the atomic ratio of Mo and Fe to S in the Fe-doped MoS_2 nanosheets approached 1:2. Carbon and oxygen were mainly derived from the conductive adhesive and absorbed oxygen molecules on the surface of the Fe-doped MoS_2, respectively.

To further confirm the existence of Fe heteroatoms in the Fe-doped MoS_2 plane, the XPS spectrum was investigated to examine the surface electronic state and composition of the Fe-doped MoS_2 nanosheets. Fig. 3(a) presents a typical overall XPS spectrum of the as-prepared samples. The chemical binding energies at approximately 229.1, 161.8, 711.5, and 532.1 eV for Mo 3d, S 2p, Fe 2p, and O 1s indicated the presence of Mo, S, Fe, and O in the Fe-doped MoS_2 nanosheets, respectively. As illustrated in Fig. 3(b), the three main peaks of Mo $3d_{3/2}$ (232.8 eV), Mo $3d_{5/2}$ (229.6 eV), and S 2s (226.7 eV) were typically characteristic of MoS_2. In Fig. 3(c), the binding energies of 161.6 and 162.6 eV corresponded to S $2p_{3/2}$ and S $2p_{1/2}$ [37], implying that Mo^{4+} and S^{2-} were dominant MoS_2 states. The Fe 2p core-level XPS spectrum (Fig. 5(d)) displayed two major characteristic peaks at 710.61 and 725.33 eV for Fe $2p_{3/2}$ and Fe $2p_{1/2}$, respectively [38]. After further peak deconvolution, four resolved peaks appeared at 708.73, 710.65, 714.85, and 724.80 eV. The peaks at 710.61 and 724.80 eV were attributed to the doped Fe^{3+}, whereas those at 708.73 and 714.85 eV were attributed to Fe^{2+}, which could form during the hydrothermal process under high temperature and pressure conditions. No signals were found for iron oxides; thus, the iron presenting on the Fe-doped MoS_2 nanosheets surface was mainly of Fe^{3+} and Fe^{2+} state, these findings agreed well with the XRD and EDS analysis of the Fe-doped MoS_2 nanosheets. Overall, the XRD, EDS mapping, and XPS characterizations suggest that Fe atoms were successfully doped into the matrix of the MoS_2.

3.2. Optical performance test

The optical properties of semiconductor materials directly affect their photocatalytic performance.

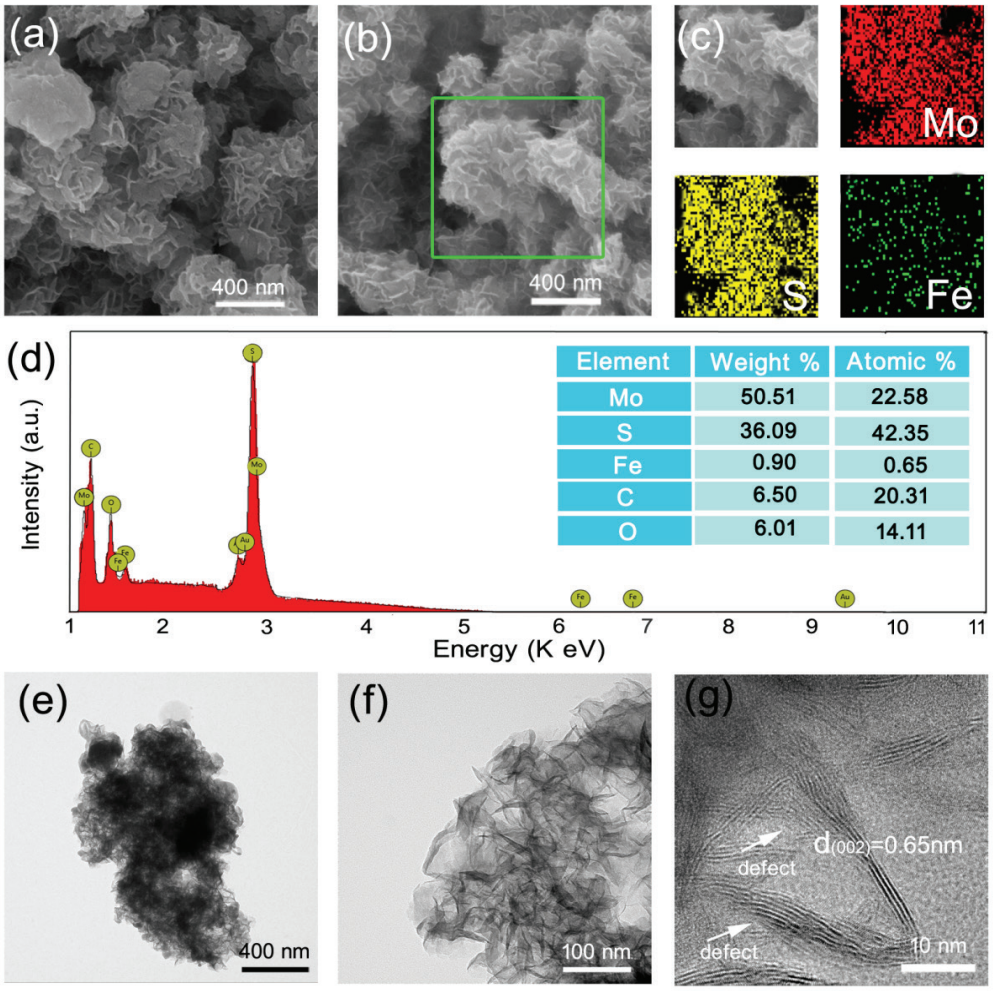

Fig. 2. SEM images of (a) pristine MoS_2 and (b) Fe-MoS_2 nanosheet, (c) element mapping and EDS results for Fe-MoS_2 nanosheets, (d) EDS analysis of Fe-doped MoS_2, ((e)–(g)) TEM and HRTEM at stand-up edges for Fe-doped MoS_2 nanosheets.

Photo-catalytic active species are mainly thought to originate from photo-generated electrons and holes. When the energy of a photon is higher than the band gap energy (E_{bg}) of the photocatalyst, it can be absorbed to promote an electron from the valence band (VB) into the CB, at which point a hole is generated in the VB. If the photo-generated electrons and holes have sufficient activity and can be effectively separated, then active species and free radicals (·OH, $\cdot O_2^-$, and $HO_2\cdot$) can be generated [9]. Therefore, the absorption spectra and mechanism of the photo-generated carriers separation and transformation play a critical role in photocatalytic reactions.

The UV–Vis absorption spectra of pristine MoS_2 nanosheets and the Fe-doped MoS_2 nanosheets are presented in Fig. 4(a). All samples exhibited maximum absorption in the visible range. Comparing the absorption spectra of un-doped MoS_2 nanosheets with those of Fe-doped MoS_2 nanosheets, the absorption intensity of Fe-doped MoS_2 nanosheets in the visible range was enhanced as the Fe doping amount increased. 5.1 at % Fe-doped MoS_2 nanosheets obtained the highest absorption intensity. The enhanced absorption spectrum implies a higher quantum yield, attributed to the impurity level introduced in the forbidden band of MoS_2 with the Fe dopant. The electron rose to the impurity level from the VB while absorbing less energy. As a result, much more visible light was absorbed, which can produce more photo-generated carriers.

To study the separation and recombination of photo-generated carriers, photocurrent responses, PL spectra, and electrochemical impedance spectroscopy (EIS) were examined for different samples (pristine MoS_2, 1.1 at % Fe-doped MoS_2, 2.9 at % Fe-doped MoS_2, 4.3 at % Fe-doped MoS_2, and 5.1 at % Fe-doped MoS_2). As shown in Fig. 4(b), all three electrodes under intermittent irradiation in the Na_2SO_4 solution demonstrated apparent photocurrent responses. The fast and uniform responses to each light on/off interval of the three photo-electrodes indicated good reproducibility of the corresponding samples. Notably, the pristine MoS_2 exhibited a relatively low photocurrent, implying low quantum efficiency. In contrast, the Fe-doped MoS_2 showed a substantially elevated photocurrent intensity compared with that of pristine MoS_2. The photocurrent is mainly thought to originate from the separation of photo-generated charges within the photo-electrode, in which electrons are transported to the back contact while

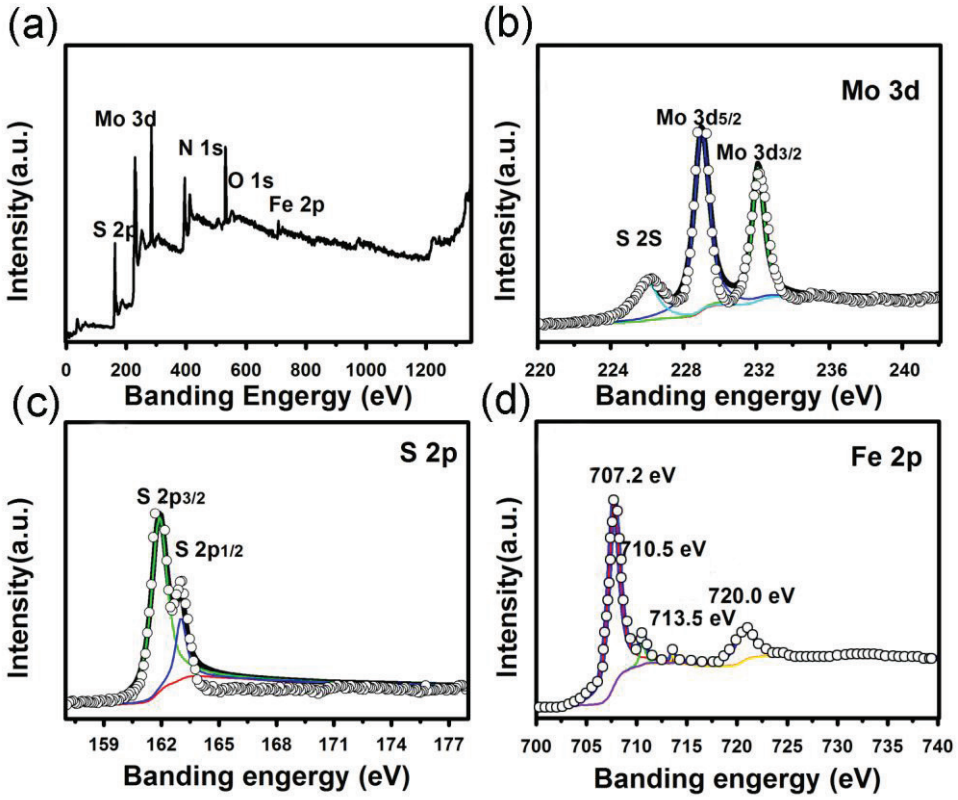

Fig. 3. XPS patterns of Fe-doped MoS_2. (a) Typical overall XPS, (b) Mo 3d and S 2s spectra, (c) S 2p spectra, (d) Fe 2p spectra.

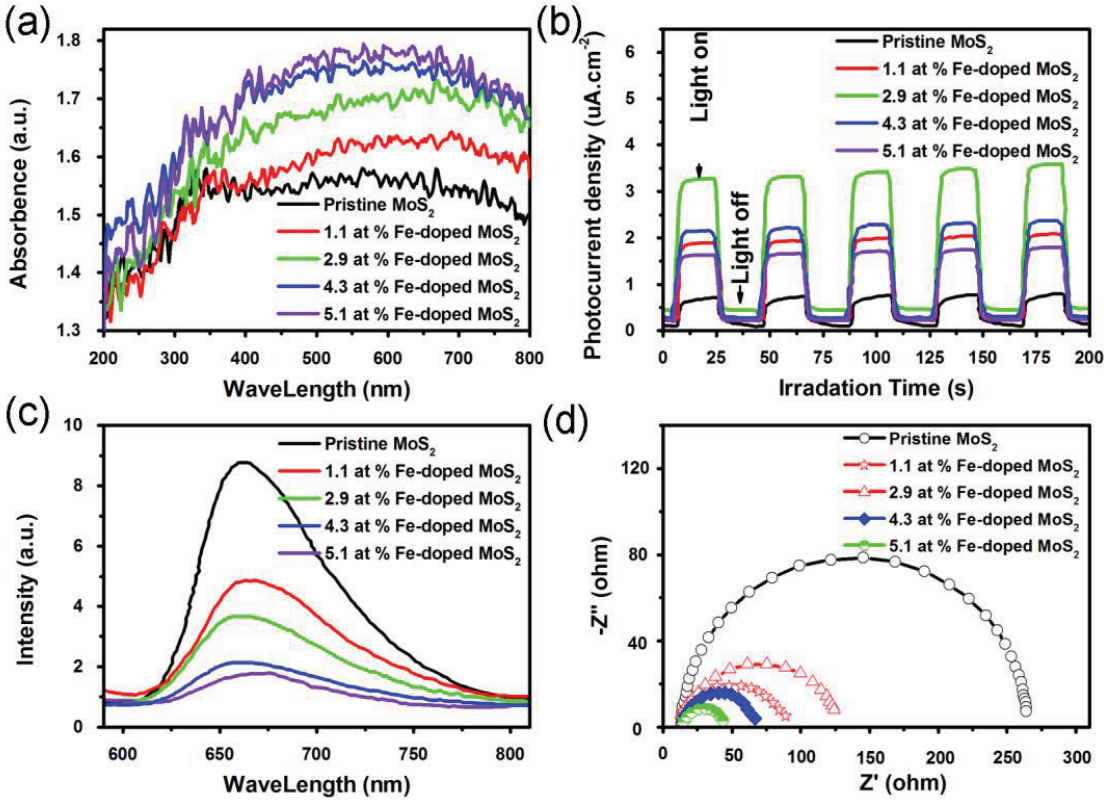

Fig. 4. (a) UV-Vis DRS, (b) transient photocurrent responses of pure MoS_2, 1.1 at % Fe-doped MoS_2, 2.9 at % Fe-doped MoS_2, 4.3 at % Fe-doped MoS_2, and 5.1 at % Fe-doped MoS_2, (c) PL emission spectra, (d) Nyquist plots of pristine and Fe-doped MoS_2 nanosheets.

holes are taken up by the holes acceptors in the electrolyte. Therefore, when the Fe-doped MoS_2 photo-anode is irradiated by light, photo-generated electrons from the excited MoS_2 are likely transferred to ITO while holes are transferred to MoS_2, resulting in as much separation of photo-generated charges as possible. A higher photocurrent response of the Fe-doped MoS_2 suggests that Fe doping positively affects the restrained recombination of photo-generated carriers; 2.3 at % Fe-doped MoS_2 obtained maximum photocurrent density. As the Fe doping amounts increased, the photocurrent density rose first and then declined because a small amount of Fe dopant trapped photo-generated electrons, facilitating the separation of photo-generated electrons and holes. However, excess Fe dopants may serve as a recombination center, hindering the photocatalytic reaction.

PL emissions are known to be due to the recombination of excited electrons and holes. A lower PL intensity may indicate a lower recombination rate of photo-generated electrons and holes under light illumination. On the contrary, a higher PL intensity may lead to a higher recombination rate of electrons and holes, exerting an adverse effect on photocatalytic performance. In this study, the PL spectra of different Fe-doped concentration MoS_2 nanosheets were tested in the range of 600–800 nm. As shown in Fig. 4(c), pristine MoS_2 nanosheets, 1.1 at % Fe-doped MoS_2, 2.9 at % Fe-doped MoS_2, 4.3 at % Fe-doped MoS_2, and 5.1 at % Fe-doped MoS_2 samples all demonstrated a broad visible light absorption band from 600 to 800 nm but exhibited clear changes in intensity. Specifically, pristine MoS_2 showed the highest PL intensity among all the samples, indicating a high recombination of electrons and holes. As hoped, the PL intensity decreased considerably when a suitable amount of Fe was doped, implying that the recombination of photo-generated carriers was effectively suppressed.

EIS is an important tool for studying the process dynamics of electrodes, surface phenomena of electrodes and measuring the conductivity of fixed electrolytes. For photocatalytic studies, the relative radius of arc on the Nyquist plot corresponds to the size of charge transfer resistance and the separation efficiency of photo-generated electron–hole pairs. Generally, a smaller curve in the EIS Nyquist plot illustrated a slenderer charge-transfer resistance [39]. As shown in Fig. 4(e), Fe-doped MoS_2 nanosheets exhibit smaller charge-transfer resistance under irradiation, suggesting the effective shuttling of charges between electrode and electrolyte, and faster interfacial charge transfer occurred, which is consistent with the results of PL spectrum and photocurrent density test.

3.3. Photo-catalytic performance test

To investigate the photocatalytic activity of hybrid materials with different amounts of Fe doping, photo-degradation of RhB tests was conducted under visible light. Photo-degradation process of RhB using pristine MoS_2 nanosheets and the as-prepared 2.9 at % Fe-doped MoS_2 nanosheets are shown in Figs. 5(a) and (b), respectively. The intensity of the maximum absorption peak for the RhB solution gradually declined with an increase in reaction time. Fig. 5(c) displays the degradation ratio of RhB using the different catalysts. The as-prepared 2.9 at % Fe-doped MoS_2 nanosheets show the highest catalytic activity, which can remove 98% of RhB dyes within 60 min. However, pristine MoS_2 nanosheets only removed 51% of RhB dyes within 60 min under visible light irradiation. Fig. 5(d) shows the kinetic plot of $-\ln (C_t/C_0)$ vs. irradiation time to examine whether the process obeyed the pseudo-first order model. A linear correlation existed between $-\ln(C_t/C_0)$ and irradiation time, demonstrating that the photo-degradation reaction of RhB followed pseudo-first order kinetics. The aim of photo-degradation is to degrade pollutions into CO_2, H_2O, and harmless minerals, rather than other intermediates. Therefore, it is necessary to study the degree of mineralization of pollutants. Therefore, the products of degradation of RhB by different catalysts prepared were studied by TOC. The test results of TOC are shown in Fig. 5(e). Despite of the TOC reduction rate is lower than the RhB decoloring rate, but the TOC rapidly decrease in photocatalytic reaction process, which indicates that the active substances first make RhB into all kinds of colorless intermediates, and then the active material completely oxidized these intermediates into CO_2, H_2O, and inorganic substances.

Fe^{3+} is known to influence electrons and trapped holes. Doped Fe^{3+} could be reduced to Fe^{2+} through photo-electron capture, thus enabling photo-electron transmission. Therefore, when a small amount of Fe^{3+} was doped, it benefitted the separation of electrons and holes and induced improved photo-degradation activity. Nevertheless, when a large amount of Fe^{3+} was doped, the distance among trappers fell sharply, and Fe^{3+} resulted in recombination centers. The trapped electrons were delivered to the holes directly, leading to low photocatalytic activity. The effects of different doping levels on photocatalytic activity were examined in this work. Compared with pristine MoS_2 nanosheets, the photo-degradation activity of the as-prepared Fe-doped MoS_2 nanosheets was obviously enhanced as indicated in Figs. 5(c) and (d). The 2.9 at % Fe-doped MoS_2 nanosheets catalysts demonstrated the most optimal performance. The enhanced photo-degradation activity of Fe-doped MoS_2 may be attributed to several factors: (1) incorporation of Fe into MoS_2 reduced the average grain size, therefore resulting in more active edge sites as confirmed by XRD and SEM results; (2) Fe dopants could be the new active sites in the basal plane of MoS_2 and help improve intrinsic conductivity, leading to significantly improved photo-degradation activity; and (3) the doped Fe^{3+}can trap photo-generated electrons and be reduced to Fe^{2+}. Fe^{2+} plays an important role as a Fenton catalyst in the decomposition of H_2O_2 and can rapidly initiate a photo-Fenton reaction in the RhB solution. Meanwhile, Fe^{2+} can be regenerated through the reduction of photo-electrons and support long-term water treatment applications.

In addition to photocatalytic performance, another important aspect of photocatalysts in practical applications is stability. Cycle runs were, therefore, conducted to evaluate the stability of samples under irradiation. In this procedure, all processes and parameters remained the same: the catalyst was recycled and washed with ethanol before being dried in a vacuum. As indicated in Fig. 5(f), Fe-doped MoS_2 nanosheets tested for degradation demonstrated a slight decline after five runs at a maximum degradation of 94.2% for the fifth run. A slight decrease in photocatalytic performance could be due to the loss of Fe-doped MoS_2 nanosheets during the recycling process. This experiment confirmed the stability of synthesized Fe-doped MoS_2 nanosheets during the photocatalytic process.

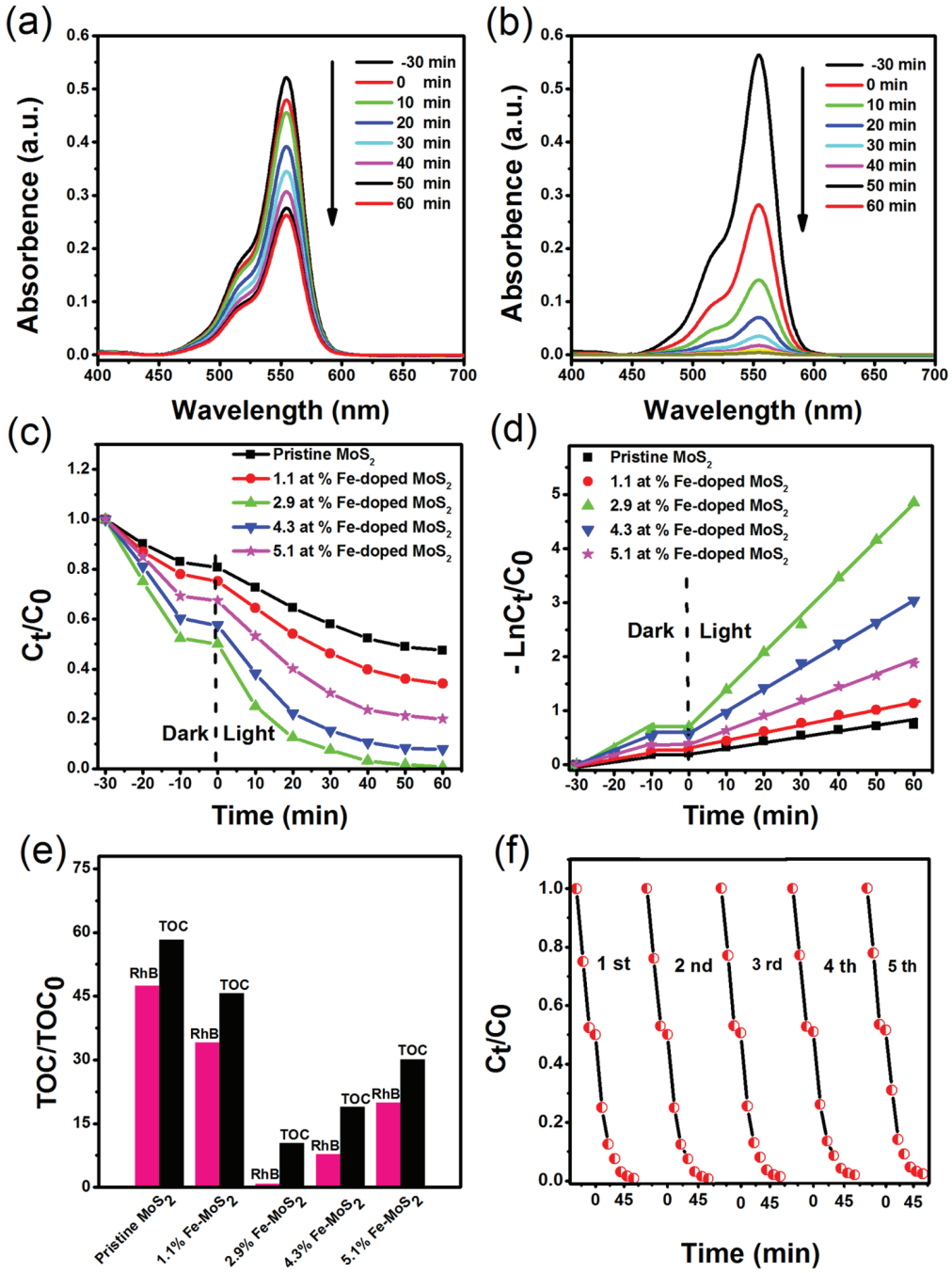

Fig. 5. Photo-degradation profiles of RhB using various photocatalysts under visible light irradiation. (a) Pristine MoS_2 nanosheets, (b) as-prepared Fe-doped MoS_2 nanosheets, ((c) and (d)) kinetic characteristics, (e) remaining TOC for the RhB dye solutions containing different catalysts, (f) catalyst reuse.

3.4. Possible mechanism for improved photocatalytic performance of Fe-doped MoS_2 nanosheets

An effective photocatalyst also relies on its band-edge positions (i.e., CB minimum and VB maximum), which determine the redox potentials of photo-generated electrons and holes [40]. In general, the more positive the VB potential, the stronger the oxidation ability of photo-generated holes [35]. By contrast, the more negative the CB, the stronger the reducing ability of photo-generated electrons. As shown in Fig. 6(a), previous studies have shown that the photo-generated electrons in CB of MoS_2 (–0.41 eV vs normal hydrogen electrode (NHE)) are sufficiently negative to reduce O_2 to generate $\cdot O_2^-$($O_2/\cdot O_2^-$ = –0.33 eV vs NHE) and reduce Fe^{3+} to generate Fe^{2+} (Fe^{3+}/Fe^{2+} = +0.77eV vs NHE). However, the ·OH radicals (·OH/H_2O = +2.27 eV vs NHE) could not be directly generated through photo-generated holes in this study because of an inadequate VB position.

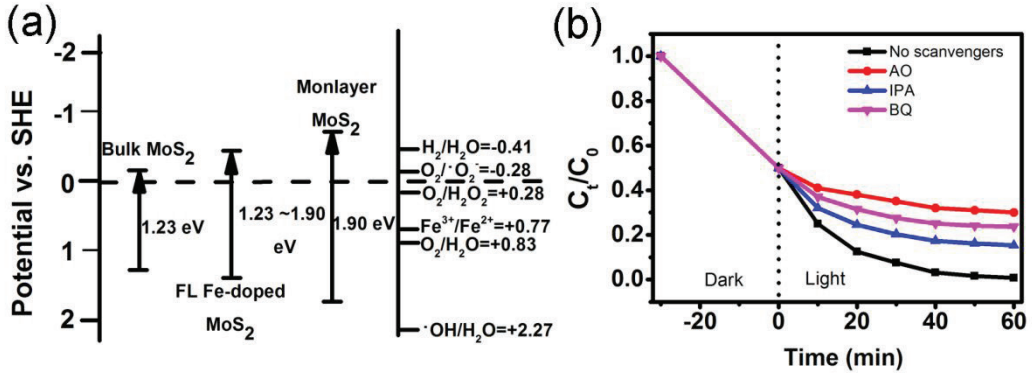

Fig. 6. (a) Potentials for various redox couples in water (pH = 7) and band-edge positions of semiconductor photocatalysts, (b) radical trapping experiments of Fe-doped MoS_2 nanosheets.

Radical trapping experiments were carried out to further confirm the above analysis of as-prepared Fe-doped MoS_2 nanosheets. OA (5 mL), BQ (5 mL), and IPA (5 mL) were used as hole (h^+), superoxide radicals ($\cdot O_2^-$), and hydroxyl radicals (·OH) scavengers to identify the main active species. As shown in Fig. 6(b), the degradation of RhB was significantly inhibited by OA, suggesting that direct oxidation by holes was critical because the potential of photo-generated holes was positive enough to effectively oxidize dyes directly. At the same time, BQ clearly reduced the photo-degradation activity of Fe-doped MoS_2 nanosheets, indicating that $\cdot O_2^-$ was an important active species for RhB degradation. Although ·OH radicals could not be directly generated through photo-generated holes, ·OH could be generated using the following approach: Fe^{2+} reacts with H_2O_2 to form ·OH. As a result, IPA suppressed the photo-degradation activity of Fe-doped MoS_2 nanosheets.

According to the above results, a possible mechanism for the heterogeneous photo-Fenton-like process is detailed in Fig. 7. First, when the energy of a photon is higher than the band gap of the energy (E_g) of Fe-doped MoS_2, it can be absorbed and promote an electron from the VB into the CB, at which point a hole is generated in the VB according to Eq. (1). Then, the photo-generated electrons react with O_2 dissolved in water and form the superoxide radical ($\cdot O_2^-$). On one hand, $\cdot O_2^-$ can suppress the recombination of photo-generated carriers; on the other, $\cdot O_2^-$ reacts with H^+ to form H_2O_2. In this study, the photo-generated electron was trapped by Fe^{3+} to form Fe^{2+}, which can accelerate the decomposition of H_2O_2 into hydroxyl radicals ·OH (i.e., Fenton reaction). At the same time, the accumulated holes on the surface of Fe-doped MoS_2 can oxidize the organic dye directly. The photo-generated electron can be trapped by Fe^{3+} to reform Fe^{2+}. In the end, these highly reactive ·OH, $\cdot O_2^-$, and h^+ will decompose RhB into carbon dioxide or other small organic molecules and water. Radical production can be expressed by the following reactions:

$$\text{Fe-doped } MoS_2 + h\nu \rightarrow e_{CB}^- + h_{VB}^+ \quad (1)$$

$$O_2 + e^- \rightarrow \cdot O_2^- \quad (2)$$

$$\cdot O_2^- + 2H^+ + e^- \rightarrow H_2O_2 \quad (3)$$

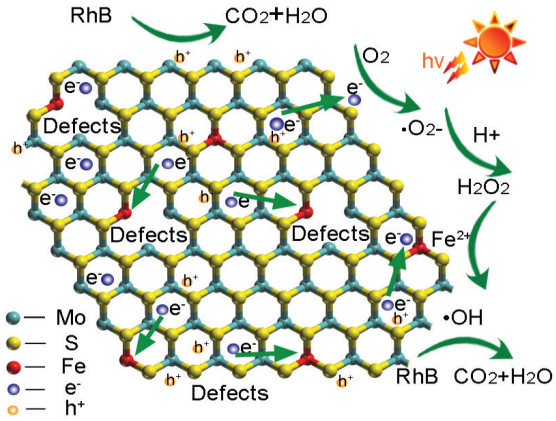

Fig. 7. Schematic diagram illustrating the mechanism of charge separation and photocatalytic reaction of Fe-doped MoS_2 nanosheets under visible light irradiation.

$$Fe^{2+} + H_2O_2 \rightarrow Fe^{3+} + \cdot OH + OH^- \quad (4)$$

$$Fe^{3+} + e^- \rightarrow Fe^{2+} \quad (5)$$

$$\cdot OH, \cdot O_2^-, h^+ + \text{RhB} \rightarrow \text{degradation products} \quad (6)$$

4. Conclusions

In summary, Fe-doped MoS_2 nanosheets with double catalytic effects were synthesized in this study using a simple hydrothermal method. Results indicate that the as-prepared Fe-doped MoS_2 nanosheets exhibited enhanced photo-degradation activity and stability in visible light irradiation compared with pristine MoS_2. This difference can be attributed to three reasons: (1) the introduction of Fe^{3+} dopants formed new active sites in the inert basal plane of MoS_2, which facilitated a traditional photocatalytic reaction; (2) doped Fe^{3+} can trap photo-generated electrons and be reduced to Fe^{2+}, thereby improving the separation efficiency of photo-generated charge carriers; and (3) a photo-Fenton-like reaction can occur during RhB degradation. Fe^{2+} can accelerate the decomposition of H_2O_2 and generate active species of ·OH, and ·OH can unselectively oxidize organics into CO_2, H_2O, and minerals. Fe^{2+} can also be endlessly regenerated

and reused, which may support long-term applications of Fe-doped MoS_2 in water treatment. The findings in this work provide a valuable reference for the design of efficient, visible-light-driven, and [14] recyclable photocatalysts for environmental mitigation of organic pollution.

Acknowledgments

The authors gratefully acknowledge financial support from the National Natural Science Foundation of China (Grants no. 61405159), the Key Project of Natural Science Foundation of Shaanxi Province (Grant no. 2014JZ2-003), Special scientific Research Project of Education Department of Shaanxi Province (Grants no. 17JK0756), and the Program for International Science and Technology Cooperation Projects of Shaanxi Province (Grants no. 2018KWZ-08).

References

[1] M.L. Marin, L. Santos-Juanes, A. Arques, A.M. Amat, M.A. Miranda, Organic photocatalysts for the oxidation of pollutants and model compounds, Chem. Rev., 112 (2012) 1710–1750.
[2] H. Djelal, C. Cornée, R. Tartivel, O. Lavastre, A. Abdeltif, The use of HPTLC and direct analysis in real time-of-flight mass spectrometry (DART-TOF-MS) for rapid analysis of degradation by oxidation and sonication of an azo dye, Arab. J. Chem., 10 (2017) S1619–S1628.
[3] D.-J. Lee, Y.-L. Cheng, R.-J. Wong, X.-D. Wang, Adsorption removal of natural organic matters in waters using biochar, Bioresour. Technol., 260 (2018) 413–416.
[4] J. Zheng, Z. Wang, J. Ma, S. Xu, Z. Wu, Development of an electrochemical ceramic membrane filtration system for efficient contaminant removal from waters, Environ. Sci. Technol., 52 (2018) 4117–4126.
[5] A. Shibata, R. Kodaka, T. Fujisawa, T. Katagi, Degradation of flumioxazin in illuminated water-sediment systems, J. Agric. Food Chem., 59 (2011) 11186–11195.
[6] C. Zhang, L. Wu, D. Cai, C. Zhang, N. Wang, J. Zhang, Z. Wu, Adsorption of polycyclic aromatic hydrocarbons (fluoranthene and anthracenemethanol) by functional graphene oxide and removal by pH and temperature-sensitive coagulation, ACS Appl. Mater. Interfaces, 5 (2013) 4783–4790.
[7] C.Y. Teh, P.M. Budiman, K.P.Y. Shak, T.Y. Wu, Recent Advancement of coagulation–flocculation and its application in wastewater treatment, Ind. Eng. Chem. Res., 55 (2016) 4363–4389.
[8] Y.H. Chuang, S. Chen, C.J. Chinn, W.A. Mitch, Comparing the UV/monochloramine and UV/free chlorine advanced oxidation processes (AOPs) to the UV/hydrogen peroxide AOP under scenarios relevant to potable reuse, Environ. Sci. Technol., 51 (2017) 13859–13868.
[9] J. Kou, C. Lu, J. Wang, Y. Chen, Z. Xu, R.S. Varma, Selectivity enhancement in heterogeneous photocatalytic transformations, Chem. Rev., 117 (2017) 1445–1514.
[10] A.T. Montoya, E.G. Gillan, Enhanced photocatalytic hydrogen evolution from transition-metal surface-modified TiO_2, ACS Omega, 3 (2018) 2947–2955.
[11] D. Ma, A. Liu, C. Lu, C. Chen, Photocatalytic dehydrogenation of primary alcohols: selectivity goes against adsorptivity, ACS Omega, 2 (2017) 4161–4172.
[12] G.P. Awasthi, S.P. Adhikari, S. Ko, H.J. Kim, C.H. Park, C.S. Kim, Facile synthesis of ZnO flowers modified graphene like MoS_2 sheets for enhanced visible-light-driven photocatalytic activity and antibacterial properties, J. Alloys Comp., 682 (2016) 208–215.
[13] E. Butanovs, A. Kuzmin, J. Butikova, S. Vlassov, B. Polyakov, Synthesis and characterization of ZnO/ZnS/MoS_2 core-shell nanowires, J. Crystal Growth, 459 (2017) 100–104.
[14] S. Lan, L. Liu, R. Li, Z. Leng, S. Gan, Hierarchical hollow structure ZnO: synthesis, characterization, and highly efficient adsorption/photocatalysis toward Congo Red, Ind. Eng. Chem. Res., 53 (2014) 3131–3139.
[15] W. Wu, J. Changzhong, V.A. Roy, Recent progress in magnetic iron oxide-semiconductor composite nanomaterials as promising photocatalysts, Nanoscale, 7 (2015) 38–58.
[16] H.J. Conley, B. Wang, J.I. Ziegler, R.F. Haglund, Jr., S.T. Pantelides, K.I. Bolotin, Bandgap engineering of strained monolayer and bilayer MoS_2, Nano Lett., 13 (2013) 3626–3630.
[17] G. Swain, S. Sultana, B. Naik, K. Parida, Coupling of crumpled-type novel MoS_2 with CeO_2 nanoparticles: a noble-metal-free p–n heterojunction composite for visible light photocatalytic H_2 production, ACS Omega, 2 (2017) 3745–3753.
[18] C. Tsai, H. Li, S. Park, J. Park, H.S. Han, J.K. Norskov, X. Zheng, F. Abild-Pedersen, Electrochemical generation of sulfur vacancies in the basal plane of MoS_2 for hydrogen evolution, Nat. Commun., 8 (2017) 1–8.
[19] H. Huang, L. Chen, C. Liu, X. Liu, S. Fang, W. Liu, Y. Liu, Hierarchically nanostructured MoS_2 with rich in-plane edges as a high-performance electrocatalyst for the hydrogen evolution reaction, J. Mater. Chem. A, 4 (2016) 14577–14585.
[20] X.L. Yin, L.L. Li, W.J. Jiang, Y. Zhang, X. Zhang, L.J. Wan, J.S. Hu, MoS_2/CdS Nanosheets-on-nanorod heterostructure for highly efficient photocatalytic H_2 generation under visible light irradiation, ACS Appl. Mater. Interfaces, 8 (2016) 15258–15266.
[21] Y. Li, H. Wang, S. Peng, Tunable photodeposition of MoS_2 onto a composite of reduced graphene oxide and CdS for synergic photocatalytic hydrogen generation, J. Phys. Chem. C, 118 (2014) 19842–19848.
[22] Q. Li, N. Zhang, Y. Yang, G. Wang, D.H. Ng, High efficiency photocatalysis for pollutant degradation with MoS_2/C_3N_4 heterostructures, Langmuir, 30 (2014) 8965–8972.
[23] N. Tian, Z. Li, D. Xu, Y. Li, W. Peng, G. Zhang, F. Zhang, X. Fan, Utilization of MoS_2 nanosheets to enhance the photocatalytic activity of ZnO for the aerobic oxidation of benzyl halides under visible light, Ind. Eng. Chem. Res., 55 (2016) 8726–8732.
[24] Y. Xue, W. Cai, S. Zheng, W. Yan, J. Hu, Z. Sun, Y. Zhang, W. Jin, W-doped MoS_2 nanosheets as a highly-efficient catalyst for hydrogen peroxide electroreduction in alkaline media, Catal. Sci. Technol., 7 (2017) 5733–5740.
[25] M.D. Xie, C.G. Tan, P. Zhou, J.G. Lin, L.Z. Sun, Ferrimagnetic half-metallic properties of Cr/Fe δ doped MoS_2 monolayer, RSC Adv., 7 (2017) 20116–20122.
[26] E.Z. Xu, H.M. Liu, K. Park, Z. Li, Y. Losovyj, M. Starr, M. Werbianskyj, H.A. Fertig, S.X. Zhang, p-Type transition-metal doping of large-area MoS_2 thin films grown by chemical vapor deposition, Nanoscale, 9 (2017) 3576–3584.
[27] X. Liu, L. Li, Y. Wei, Y. Zheng, Q. Xiao, B. Feng, Facile synthesis of boron- and nitride-doped MoS_2 nanosheets as fluorescent probes for the ultrafast, sensitive, and label-free detection of Hg(2+), Analyst, 140 (2015) 4654–4661.
[28] K.V. Baiju, C.P. Sibu, K. Rajesh, P.K. Pillai, P. Mukundan, K.G.K. Warrier, W. Wunderlich, An aqueous sol–gel route to synthesize nanosized lanthana-doped titania having an increased anatase phase stability for photocatalytic application, Mater. Chem. Phys., 90 (2005) 123–127.
[29] X. Sun, C. Li, L. Ruan, Z. Peng, J. Zhang, J. Zhao, Y. Li, Ce-doped SiO_2@TiO_2 nanocomposite as an effective visible light photocatalyst, J. Alloys Comp., 585 (2014) 800–804.
[30] J.W. Shi, J.T. Zheng, P. Wu, Preparation, characterization and photocatalytic activities of holmium-doped titanium dioxide nanoparticles, J. Hazard. Mater, 161 (2009) 416–422.
[31] X.S. Nguyen, G. Zhang, X. Yang, Mesocrystalline Zn-doped Fe_3O_4 hollow submicrospheres: formation mechanism and enhanced photo-Fenton catalytic performance, ACS Appl. Mater. Interfaces, 9 (2017) 8900–8909.
[32] S. Guo, G. Zhang, J.C. Yu, Enhanced photo-Fenton degradation of rhodamine B using graphene oxide-amorphous FePO(4) as effective and stable heterogeneous catalyst, J. Colloid Interface Sci., 448 (2015) 460–466.
[33] C. Xiao, J. Li, G. Zhang, Synthesis of stable burger-like α-Fe_2O_3 catalysts: formation mechanism and excellent photo-Fenton catalytic performance, J. Cleaner Prod., 180 (2018) 550–559.
[34] W. Li, Y. Tian, P. Li, B. Zhang, H. Zhang, W. Geng, Q. Zhang, Synthesis of rattle-type magnetic mesoporous Fe_3O_4@mSiO_2@

BiOBr hierarchical photocatalyst and investigation of its photoactivity in the degradation of methylene blue, RSC Adv., 5 (2015) 48050–48059.
[35] P. Liu, Y. Liu, W. Ye, J. Ma, D. Gao, Flower-like N-doped MoS_2 for photocatalytic degradation of RhB by visible light irradiation, Nanotechnology, 27 (2016) 1–8.
[36] Z.J. Yu, M.R. Kumar, Y. Chu, H.X. Hao, Q.Y. Wu, H.D. Xie, Photocatalytic decomposition of RhB by newly designed and highly effective CF@ZnO/CdS hierarchical heterostructures, ACS Sustain. Chem. Eng., 6 (2017) 155–164.
[37] J. Zhang, L. Huang, Z. Lu, Z. Jin, X. Wang, G. Xu, E. Zhang, H. Wang, Z. Kong, J. Xi, Z. Ji, Crystal face regulating MoS_2/TiO_2 (001) heterostructure for high photocatalytic activity, J. Alloys Comp., 688 (2016) 840–848.
[38] X. Wang, M. Hong, F. Zhang, Z. Zhuang, Y. Yu, Recyclable nanoscale zero valent iron doped g-C_3N_4 for efficient photocatalysis of RhB and Cr(VI) driven by visible light, ACS Sustain. Chem. Eng., 4 (2016) 4055–4063.
[39] K. Wang, G. Zhang, J. Li, Y. Li, X. Wu, 0D/2D Z-scheme heterojunctions of bismuth tantalate quantum dots/ultrathin g-C_3N_4 nanosheets for highly efficient visible light photocatalytic degradation of antibiotics, ACS Appl. Mater. Interfaces, 9 (2017) 43704–43715.
[40] Z. Wang, B. Mi, Environmental applications of 2D molybdenum disulfide (MoS_2) nanosheets, Environ. Sci. Technol., 51 (2017) 8229–8244.